MODELING LIGHT SCATTERING PROFILES AS THEY RELATE TO MITOCHONDRIAL MORPHOLOGICAL CHANGES DURING ALZHEIMER'S DISEASE

Stefan Sierra

BME 679H
Special Honors in Biomedical Engineering
Submitted to fulfill the Plan II Honors Program thesis requirement
The University of Texas at Austin

11 May 2017

_____
H. G. Rylander III
Biomedical Engineering
Supervising Professor

_____
Thomas Milner
Biomedical Engineering
Second Reader

ABSTRACT

Author: Stefan Sierra

Title: Modeling light scattering profiles as they relate to mitochondrial morphological changes during Alzheimer's disease

Supervising Professors: H. G. Rylander III, Thomas Milner

Every 66 seconds someone in the United States develops Alzheimer's disease. Today, 24 million people are living with the disease. Alzheimer's is a terminal illness without a cure. Unfortunately, no non-invasive diagnostic technique exists that can definitively diagnosis an individual with early-stage Alzheimer's. Most often, those that are given "probable" diagnoses are properly diagnosed only after irreversible damage has occurred in the brain. An earlier diagnosis would have brought these patients a variety of benefits. An early diagnosis means that a patient is afforded earlier access to available treatments, is able to build a care team, can investigate support services and can enroll in potentially effective clinical trials. Aside from physical benefits, early-diagnosed patients can better prepare emotionally, socially, financially and legally for the toll the disease takes on the body and mind. Thus, an unmet need exists to develop a diagnostic technique that can definitively diagnose Alzheimer's as early as possible.

Altered brain energetics and metabolism have been shown to be associated with Alzheimer's disease. These changes occur alongside alterations of the normal cycles of fission and fusion of mitochondria in neurons, which together are referred to as mitochondrial dynamics. Changes in mitochondrial dynamics lead to inadequate cellular energy production, ultimately inducing the loss in synaptic activity and neuronal death associated with Alzheimer's.

This research involved creating a Monte Carlo model that simulates the mitochondrial morphological changes that occur in response to the progression of neurodegenerative diseases like Alzheimer's. Simultaneously, the model predicts light scattering profiles for a specific mitochondrion as it undergoes the structural changes associated with altered mitochondrial dynamics.

This model serves to provide useful insight into optical imaging of mitochondrial dynamics and how optical imaging technology/processing might be optimized to provide useful diagnostic information for Alzheimer's and other forms of dementia.

Table of Contents

1 Introduction

1.1 Undergraduate Motivation

In my third year at the University of Texas at Austin, I took two semesters of Quantitative Engineering Physiology. The first semester was co-taught and one of my professors was Dr. Rylander, who is my thesis advisor and lab director. One of the units Dr. Rylander taught was neurology and neurological diseases, and I found that specific unit to be the most exciting. In class, we discussed several imaging techniques, including Optical Coherence Tomography (OCT), and how those techniques affect diagnosis and treatment of diseases. After the class ended, I contacted Dr. Rylander about working in his lab and have been involved with his research since. Working with Drs. Rylander and Milner led me to the current project I have taken on.

Stefan Sierra 5/16/2017 10:25 AM
Deleted: jointly

1.2 Research Inspiration

The research I am working on was inspired by the technology currently being optimized and utilized in the lab for imaging, namely Optical Coherence Tomography (OCT). The lab team had been investigating OCT as a potential imaging tool with which one could diagnose Alzheimer's disease prior to my arrival. A key limitation the lab faces is obtaining accurate, reusable physical models of tissue that has undergone neuronal degradation and corresponding mitochondrial fission. Mice models have been used previously, but physical/experimental results need to be interpreted in the context of expected and controlled results.

1.3 Research Target

The goal of my research was to create the "expected, controlled results" that might be used for benchmarking experimentally acquired results. The first component of my work was creating

a model with relevant physiological parameters that could predict how light would interact with a single sphere, utilizing Mie Theory (to be discussed). This could tell us how light interacts with an individual mitochondrion. The second component of my research was creating a Monte Carlo model that demonstrates the process of mitochondrial fission during Alzheimer's disease, given certain inputs. The objective was to incorporate "memory" so that we could effectively model and track individual mitochondria in a person affected by the disease. Finally, the two models can be used together to demonstrate how overall mitochondrial morphology evolves during Alzheimer's disease and how light interactions change in response.

2 Significance and Description of the Problem

2.1 The Prevalence of Alzheimer's Disease

Today, Alzheimer's disease affects approximately 24 million individuals and current estimates predict a quadrupling of this figure by 2050[1]. Every 66 seconds someone in the United States develops Alzheimer's. This high incidence rate means that approximately five million Americans are living with the disease, and that number is projected to grow to 16 million over the next 30 years. Alzheimer's is a terminal illness and is the sixth leading cause of death in the United States[2]. The growth of these figures in the United States is in large part due to the aging of the massive "baby boom" generation[3]. In 2010 only 13% of the U.S. population was aged 65 and over, but the "baby boom" generation is so large that the percentage of the population aged 65 and over is expected to be over 20% in 2030[4].

Age is the best-known risk factor for Alzheimer's disease, so an aging population is a strong cause for concern[5]. The impact on the overall health of the population is not the only problem that an aging population poses. The economic burden of the disease is equally troubling

and will only become more so as the prevalence increases. Alzheimer's has been found to have higher health care costs than any other disease. In the last five years of life, total health care spending per afflicted patient averages over a quarter million dollars. This cost is 57% greater than other diseases, including cancer and heart disease[6]. This year, in the United States alone, Alzheimer's and other forms of dementia will cost the nation 259 billion dollars. Medicaid and Medicare will cover approximately $175 billion, or 67 percent, of this figure. By 2050, these costs could rise to 1.1 trillion, which translates to a fourfold increase in government spending related to the disease[2].

2.2 The Prognosis of Alzheimer's Disease

According to the Alzheimer's Association, Alzheimer's disease can generally be described as having three broad stages: mild (early-stage), moderate (middle-stage) and severe (late-stage). Symptomatic determination of a particular disease phase is challenging because symptoms often overlap and are so variable between afflicted individuals. The disease is known to be terminal, but progresses at rates variable by person. The typical life expectancy upon diagnosis is six to eight years, but some individuals have been known to live twenty years after diagnosis. Thus, life expectancy is quite difficult to determine upon initial diagnosis and most often is projected based on the severity of symptoms and the rate at which they are progressing over time within the specific patient[7].

An unofficial stage of the disease exists known as the preclinical phase. In this phase, degenerative changes in the brain, like those to be discussed in the next section, are occurring but symptoms have not yet started to present themselves. These degenerative changes in the brain can begin up to a decade prior to the appearance of symptoms[8].

The first stage of Alzheimer's disease is known as mild Alzheimer's or the early-stage. In

this stage, cognition and memory are primarily affected but the afflicted individual is often able to continue with daily work and social activities. Often times, individuals in this stage face problems determining the right word for certain objects. They might also struggle with locating everyday objects. They will often forget the names of new people and can have difficulty concentrating, planning and organizing[7]. Family members and close friends often become aware of these changes. But, these symptoms might be overlooked, as common forgetfulness amongst the elderly is the accepted social norm[9]. This is especially problematic because a late diagnosis might be detrimental.

The second stage of Alzheimer's disease is moderate Alzheimer's or the middle-stage. The middle-stage is generally the longest of the three phases and can last many years. Over the course of this stage, the patient will become increasingly dependent on a caregiver. The cognitive decline in the middle-stage is much greater than in the early-stage. Individuals will begin to forget important details about family members and friends, including names and faces. They also begin to forget details of their own personal history. They have trouble remembering important details like their phone number or addresses, which is dangerous because there is also an increased risk of wandering or getting lost. They begin to require help with daily tasks like getting dressed for appropriate weather conditions. Physical symptoms may also present themselves. For instance, some individuals with moderate Alzheimer's notice changes in sleep patterns and some become incontinent[7].

The final stage of Alzheimer's disease is known as severe Alzheimer's or the late-stage. This stage is characterized by acute, critical physical changes. Individuals in this stage will experience difficulty walking, sitting and eventually swallowing. Memory and cognition are affected greatly and significant personality changes result. Patients will need constant medical

supervision and care during this stage. Additionally, late-stage individuals become more susceptible to infections, especially pneumonia[7]. One study found that approximately 40% of late-stage Alzheimer's patients die as a result of infection, specifically bronchopneumonia[10]. Near the end of this phase, the patient will most likely be bed-ridden while the body shuts down[8].

2.3 The Physiology of Alzheimer's Disease

The physiology and epidemiology of Alzheimer's disease is quite complicated, which is why the task of diagnosis is such a challenging one. Examination of brain tissue post-mortem under a microscope, during a procedure like an autopsy, can allow us to look for the two physiological hallmarks of the disease, namely neurofibrillary tangles and amyloid plaques. Neurofibrillary tangles are essentially bundles of fibers that consist of tau protein. Amyloid plaques appear like clumps, and consist of beta-amyloid protein[8]. Figure 1 below depicts brain tissue in healthy individuals and in Alzheimer's patients after the development of neurofibrillary tangles and amyloid plaques[11].

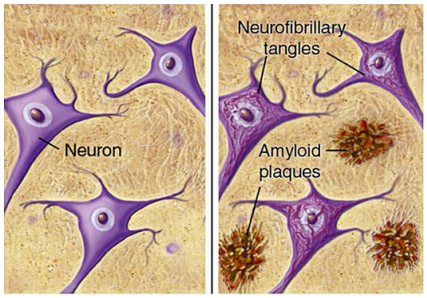

Figure 1: Healthy (left) vs. Alzheimer's Disease (right) Brain Tissue
Source: BrightFocus Foundation

Neurofibrillary tangles almost always exist in Alzheimer's patients. The number of neurofibrillary tangles is closely tied to the level of disease progression, with a higher number of tangles corresponding to a more advanced disease state. This trend implies a correlation between the formation of neurofibrillary tangles and neuronal dysfunction. As stated previously, the

tangles consist of tau protein. But, the tau protein involved is unique in that it is highly phosphorylated. The presence of phosphorylated tau protein and corresponding neurofibrillary tangles is associated with problems in the microtubule networks of neurons. Specifically, there are key disturbances in the microtubular network that in turn produce disruptions in axoplasmic transport, the necessary movement of cellular components within a neuron[12].

The general term amyloid refers to the protein fragments that the body naturally produces. But, beta-amyloid refers to a protein fragment "snipped" from an amyloid precursor protein (APP). In a healthy person, these fragments are degraded and removed. In patients with Alzheimer's disease or other forms of dementia, these fragments coalesce to form hard, insoluble plaques[11]. Unlike for neurofibrillary tangles, it was challenging for scientists to find a direct link or correlation between concentration of amyloid plaques and the level of disease progression. However, recent research indicates that amyloid plaque solubility is the correlated physiological factor[13].

While neurofibrillary tangles and amyloid plaques are considered the physiological hallmarks of Alzheimer's disease, recent research reveals a strong connection between altered brain energetics and metabolism with the disease. Specifically, significant hypometabolism, a term meaning abnormally low metabolic rates, has been detected early in Alzheimer's patients via ^{18}F-fluorodeoxyglucose positron emission tomography (F-PET) scans. This suggests that abnormal energy metabolism underlies the development and progression of the disease[14].

Neurons require robust energy production to maintain normal synaptic activity, to remain healthy and to survive. It is well known that mitochondria are the "powerhouse" of the cell. Thus, by definition, it is mitochondria that are responsible for the robust energy production that allows neurons to behave normally and survive. Mitochondria have to perform very specific

tasks in order to maintain an adequate amount of energy production. Recent studies reveal that one of these tasks mitochondria must perform is undergoing constant cycles of fission and fusion, collectively termed "mitochondrial dynamics"[15–17].

The cellular machinery involved in performing the processes related to mitochondrial dynamics is very sensitive and depends on the fidelity of various proteins. Proteins that have been identified that influence mitochondrial dynamics include: dynamin related protein 1 (Drp1), mitochondrial fission protein 1 (Fis1), mitochondrial fission factor (Mff), mitofusin-1 and mitofusin-2 (Mfn1, Mfn2), and optical atrophy 1 (Opa1) protein. Levels of the aforementioned proteins affect how overall mitochondrial morphology shifts in response to the energetic demands of the cell by dictating whether fission or fusion will occur[15,18–22].

Fission and fusion normally occur together in a balanced fashion with fusion being more common than fission. But, excessive fission has been observed in cellular and animal models of Alzheimer's disease as well as in afflicted patients[23]. Normally, mitochondrial fission is a process that is essential for quality control ensuring that damaged or old organelles can be removed via mitophagy,[15] a process that involves the engulfment of mitochondria by a phagophore and subsequent degradation to allow for a "recycling" of organellar parts[24]. Moreover, this fission process results in the consolidation of the "still-intact functional elements of mitochondria," while simultaneously segregating dysfunctional mitochondrial components into "depolarized daughter organelles that are targeted for mitophagy"[25]. While mitochondrial fission enables quality control, mitochondrial fusion preserves mitochondrial function and subsequent cell energy production. Contemporary research indicates that a highly fused arrangement of mitochondria is a cellular response to energy deprivation and stressful environmental conditions[26]. This fused arrangement provides stress resistance and prevents

mitophagy[27,28]. So, it seems fusion prevents mitophagy while fission enables it. This idea offers an explanation for the balance of fission and fusion normally observed, where higher rates of fusion exist. Because mitochondria can have satisfactory life cycles, they need not be degraded as often as they need be preserved[29].

The relationship between mitochondrial dynamics and the onset of Alzheimer's disease is still being studied extensively. A recent study suggests that Alzheimer's disease may be primarily a vascular disease where brain amyloid deposition is correlated with midlife vascular risk factors like high Body Mass Index (BMI), hypertension and diabetes. The study supposes that vascular problems create hypoxic stress in the brain, which then induces the aforementioned changes in mitochondrial dynamics. This altered balance leads to neuronal energy deficiencies and subsequent cell death[30]

Figure 2 below depicts three common mitochondrial morphologies found in a study by Zhang et al, where arrows indicate mitochondria. Each of the images was visualized using standard TEM and super-resolution immunofluorescence[29]. Image A corresponds to the prevalent mitochondrial structure in healthy individuals. Images B and C represent the two most common morphologies present during Alzheimer's.

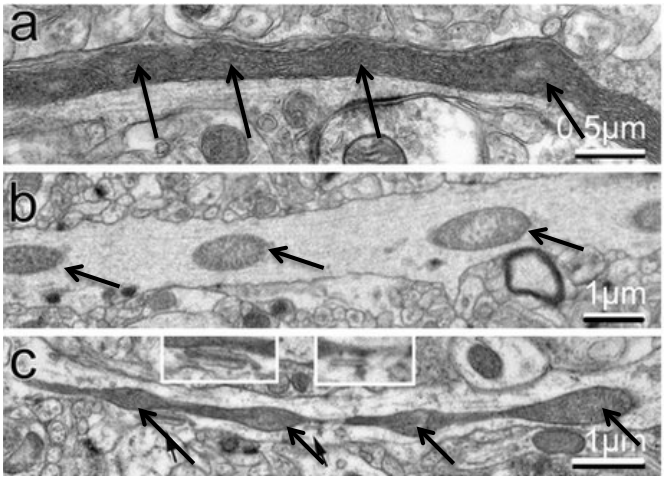

Figure 2: Images of Mitochondrial Morphologies Found in Healthy Individuals (A) and Individuals with Alzheimer's Disease (B/C); Source: Zhang et al.

Image A shows the more common, fused state that is prevalent in healthy individuals. Image B shows severely disjointed mitochondria, as would exist during Alzheimer's disease when net fission is occurring. The Zhang et al study argues that the morphology shown in Image C is a precursor to the morphology present in Image B, and that it is the cell's final attempt to preserve its energy production by having loosely connected mitochondria that are less susceptible to mitophagy[29].

Furthermore, it appears that states of mitochondrial fission and fusion are both physically adaptive and required, especially in situations of metabolic stress or energy deprivation. But, it is clear that issues arise when more mitochondria are in a state of fission than fusion, as is the case with Alzheimer's disease. The largest issue is that a higher proportion of mitochondria in a state of fission translates to excessive rates of mitophagy. This increased rate of mitophagy in turn creates a higher proportion of degraded, non-functional mitochondria and a corresponding inadequate number of intact, functioning mitochondria. Fewer functioning mitochondria means decreased energy production. Insufficient energy production leads to loss of synaptic activity and neuronal death, two conditions involved in the onset and progression of Alzheimer's disease[29].

2.4 Current Diagnostic Techniques/Treatments for Alzheimer's Disease

There are two potential preliminary diagnoses that can be made if a patient seeks medical attention for symptoms like memory problems. These are "possible Alzheimer's dementia" and "probable Alzheimer's dementia." Possible Alzheimer's dementia differs from probable Alzheimer's dementia in that the dementia "might be due to other causes," where in the case of probable Alzheimer's dementia "no other cause for dementia can be found"[8].

The diagnostic technique for Alzheimer's disease is rather crude and almost subjective in a sense. Physicians will perform an array of tests and analyses to determine if someone has

probable or possible Alzheimer's. First, the physician will investigate the patient's overall medical history and will inquire about any recently observed changes in behavior, memory or personality with the patient and, if possible, the patient's family and friends. Next, the physician may conduct some cognitive testing, like tests of memory, problem solving, language and attention. After that, the physician will carry out standard medical tests like urine and blood sampling. If necessary, the physician might also perform various types of brain scans (CT, PET, MRI, etc). The latter two testing procedures are completed to rule out any other potential causes for the disease, like vascular dementia[8].

All of this testing leaves the patient with only one type of conclusion – an uncertain one. The uncertainty rests in the inability of current diagnostic techniques to definitively ascertain whether or not a patient is affected by Alzheimers. Unfortunately, the only time we can accurately and *definitively* diagnose a patient with Alzheimer's is post-mortem, during an autopsy, when clinical measures can be linked with an examination of brain tissue under a microscope.

Currently, no cure for Alzheimer's disease is available. However, some current medical technologies and practices are being used to preserve mental function, manage symptoms and potentially slow or delay the onset of symptoms while the disease progresses. A few medications have been approved by the FDA for use in human patients afflicted by Alzheimer's. Medications that have shown efficacy in treating mild to moderate Alzheimer's include: donepezil, rivastigmine, and galantamine. Effective medications for moderate to severe Alzheimer's include donepezil and memantine. All of the previously listed drugs work by modulating neurotransmitters. While these medications have been shown to be effective in reducing symptoms they do not change the underlying disease pathology. Additionally, they are not

effective for all patients and may help some patients for only a limited time[8].

2.5 Future of Diagnostic Techniques and Benefits of Early Diagnosis

Scientists around the world are investigating various novel diagnostic techniques and strategies. Some diagnostic techniques being studied that have shown promise in diagnosing Alzheimer's early include: cerebrospinal fluid (CSF) protein testing, functional imaging and molecular imaging. Each technique varies in its approach and has specific drawbacks[31].

Testing of cerebrospinal fluid (CSF) proteins appears promising. This procedure involves a sampling of CSF via a lumbar puncture. The levels of certain proteins, specifically tau and beta-amyloid, are then examined in that CSF sample. Because research suggests that these proteins accumulate and are prevalent in the earlier stages of Alzheimer's, these levels could help physicians determine if a patient is developing Alzheimer's[31]. However, two key issues are associated with this technique. The first is the invasiveness of the procedure. Most patients do not seek medical attention until symptoms appear, and those that do will likely be averse to a diagnostic lumbar puncture. This makes detection at the earliest stages, before severe and irreversible damage to the brain occurs, less likely. The second limitation is that "analysis of protein levels in the same sample often varies significantly from institution to institution"[31]. Thus, achieving consistent measurement and analysis to have meaningful results remains a challenge.

Functional imaging is also being explored as a potential diagnostic tool. As mentioned previously, alterations in brain metabolism and activity have been observed in patients with Alzheimer's. One study using F-PET imaging showed that Alzheimer's disease is often associated with hypometabolic activity (reduced use of glucose) in brain areas involved in memory, learning and problem solving[14]. So, functional imaging could be used to detect changes

in brain metabolism, which starts to occurs in the earliest stages (preclinical) of Alzheimer's. However, this technique has one key limitation, namely the lack of confirmed information needed for scientists to draw connections between the observed activity patterns and diagnostic information[31].

Another imaging technique, molecular imaging, is also being investigated as a diagnostic tool. This technique has the potential to diagnose Alzheimer's before the disease permanently alters a patient's brain structure or function. Molecular imaging relies on molecular markers that adhere to relevant pathological molecules, proteins or tissues. For instance, one specific radiotracer, known as Pittsburgh compound B (PIB), is capable of highlighting beta-amyloid deposits. This technique is minimally invasive, but is limited by the pace of molecular marker discovery. Also, those molecular markers that do exist might not be entirely useful for diagnostic purposes. For instance, beta-amyloid concentration is not directly correlated with a level of disease progression, so the benefit of marking that specific protein is limited[31].

The race to discover an accurate technique or effective tool that can diagnose Alzheimer's at its earliest stages is very important. There are a multitude of benefits that can be derived from an early diagnosis. Firstly, the patient is afforded earlier access to available treatments, is able to build a care team, can investigate support services and enroll in potentially effective clinical trials. Aside from the physical benefits, early-diagnosed patients can better prepare emotionally, socially, financially and legally for the toll the disease takes on the body and mind[32].

Approximately 89% of Americans say they would want to know if they had Alzheimer's if they were experiencing confusion or memory loss, but less than half of Americans living with Alzheimer's are aware they have the disease[32]. So, it is clear that our current diagnostic techniques fall short and that a more effective diagnostic tool would be well received.

3 Approach to Diagnosis via Optical Coherence Tomography

3.1 Optical Coherence Tomography as an Imaging Technique

Optical Coherence Tomography (OCT) is a relatively new imaging technique that allows for high-resolution, cross-sectional imaging. OCT is similar to ultrasound in function, but utilizes light instead of sound to generate images. OCT has been shown to be useful in imaging microstructures present in biologic systems, and operates by measuring backscattered light. The images produced by OCT systems are essentially "two-dimensional data sets, which represent optical backscattering in a cross-sectional plane of tissue"[33].

There are many advantages to using OCT as an imaging technique. Image resolutions of 1 to 15 µm can be achieved, which is one to two orders of magnitude higher than typical ultrasound technology. In addition, imaging can be performed *in situ* and in real time. The ability to image tissue *in situ* and in real time means that OCT can serve as a sort of optical biopsy. The traditional method of determining tissue changes that result from disease is the removal of tissue and subsequent microscopic examination. So, for the aforementioned reasons, OCT might be a good substitute for excisional biopsies in cases where tissue excision is dangerous or impossible. In addition, OCT imaging can reduce the sampling errors associated with excisional biopsies[33].

The first applications of OCT imaging were in the field of ophthalmology. OCT is

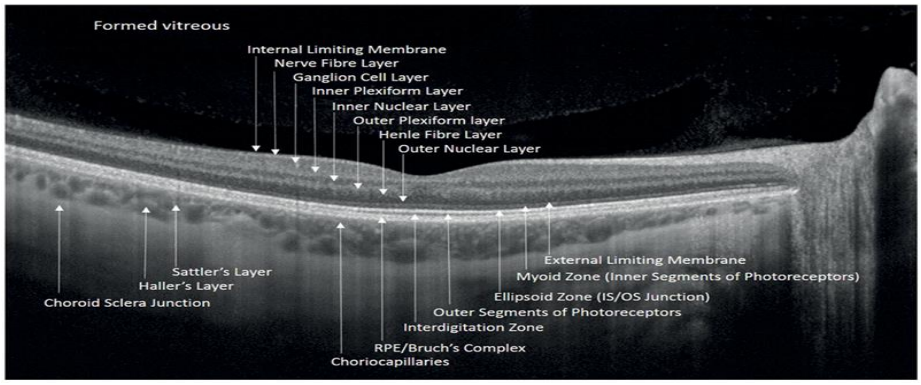

Figure 3: Visualization of retinal layers, imaged by Swept-Source OCT (SS-OCT); Source: Optician

especially useful in this field because the technology enables noncontact, noninvasive imaging of the anterior eye and of morphologic features of the human retina. Figure 3 above is an OCT scan of a human retina. The image reveals the high resolution OCT imaging can provide and how detailed microstructures can be differentiated[34]. Optical imaging of the retina at this level is normally very difficult because of the retina's transparency and extremely low levels of optical backscattering. However, OCT imaging is highly sensitive and allows these poor backscattering features to be visualized.

In all, there are several key biomedical applications of OCT. The first has already been noted, which is the ability of OCT to image at high resolutions revealing morphology and allowing some cellular features to be resolved. Second, OCT can image directly through the air without needing to make contact with the tissue of interest, representing a key advantage over ultrasound. Because OCT can image *in situ*, sampling errors can be reduced due to enhanced coverage. Additionally, real-time imaging provides real-time diagnostic potential.

3.2 Mitochondrial Imaging via Optical Coherence Tomography

Our lab is investigating OCT as a tool by which to early diagnose Alzheimer's. This would involve observing the aforementioned morphological changes of mitochondria that occur because of the disease. Detecting mitochondrial structure in vivo is a unique challenge, because of the small size of mitochondria, which have diameters of approximately 0.75 μm[35]. This particle size is beyond the resolution of most imaging techniques. However, mitochondria have interesting properties that make them appealing candidates for optical imaging. Specifically, mitochondria have distinctive light scattering characteristics. Imaging mitochondria specifically in the retina is even more useful in the context of diagnosing Alzheimer's because of the relationship between the brain and the optic nerve. We know that the optic nerve is

embryonically derived from the forebrain and also enclosed by the meninges, the three membranes that envelop the brain and spinal cord. For these reasons, many scientists increasingly view the eye as the "window to the brain"[36,37]. In addition, recent research suggests that retinal changes occur alongside brain changes during neurodegenerative disease, like Alzheimer's[36,38–40]. Furthermore, OCT imaging would be a useful tool to monitor changes in mitochondrial dynamics occurring in "brain tissue" during Alzheimer's, since the technique is already widely used to image the retina and because the retina is closely related to the brain. However, standard OCT systems are unable to image mitochondrial morphology with sufficient resolution.

A previous study conducted in the lab I have been working in, the Biomedical Engineering Laser Laboratory (BELL), at the University of Texas at Austin attempts to resolve this issue of resolution. The study involved optimizing the design and construction of a scattering-angle resolved OCT system (SAR-OCT) to better investigate the optical properties of healthy human retinas[41]. The study concluded that ocular regions with "lower retinal ganglion cell density" were correlated with the SAR-index. Further, the lab has demonstrated that sub-resolution light scattering variations in the retina can be detected. This means that the lab has the potential, using SAR-OCT, to observe the sub-resolution light-scattering variations that are a product of mitochondrial structural changes during neurodegenerative diseases like Alzheimer's.

3.3 Split-Spectrum SAR-OCT

Split-spectrum (SS) SAR-OCT is an imaging process technique that can be utilized to derive information about how scattering properties of light are influenced by the size of scatterers in a medium. In terms of our research, SS-SAR-OCT could be useful in determining the size of mitochondria (the scatterer) in the retina (the medium). SS-SAR-OCT would involve

probing the retinal sample at different wavelengths to identify the wavelength dependence of the dispersed scatterers, which in my study are mitochondria. According to Mie Theory, the scattering profile of light around a spherical object that has a size close to the incident light's wavelength will be wavelength-dependent. This means that a new SAR index (SARi) could be calculated for various spectra. Taking the mean of the second derivative of the SARi (SARi'') would then allow us acquire information about the concavity, or curve directionality, of the scatterer's dependence on wavelength. This is possible because a second derivative of a function indicates its concavity. Further, we could use SARi'' to map a trend that would help in observing the relevant sub-resolution light-scattering variations, which could potentially point to mitochondrial structure and help us relate that structure to a relevant disease state.

4 Monte Carlo Modeling of Mitochondrial Fission

4.1 Monte Carlo Model Relating Mitochondrial Structure and Scattering Profiles

My individual research had two major components. The first was building a Monte Carlo model that simulates mitochondrial morphological changes as they occur during Alzheimer's disease. The second component involved creating a computer program that predicted light scattering profiles of a sphere according the Mie Theory.

4.1.1 Monte Carlo Model

My early research suggested that no complex computational models existed that accounted for changing mitochondrial dynamics during neurodegenerative diseases. There have been images generated computationally that depict mitochondrial morphology in states of fission and fusion, respectively[29,42]. But, none of these images incorporated "memory." By that I mean there

were no models that generated a set of mitochondrial chains and then manipulated those specific chains to simulate how a neurodegenerative disease would progress over time. So, I set out to create a Monte Carlo model that forecasted changes that occur to overall mitochondrial morphology as a result of Alzheimer's.

Monte Carlo simulations are useful in their own right because they allow a user to input certain parameters and then output probable outcomes according to those parameters. To build a Monte Carlo simulation for changing mitochondrial dynamics, I did a literature search to get a better understanding of what happens to mitochondria during neurodegenerative diseases like Alzheimer's. It became clear that fission and fusion occur together and randomly, with more fission events occurring during Alzheimer's than in normal tissue[23,29,43]. In addition to separating from one another, mitochondria also experience a decrease in diameter and an increase in index of refraction (IOR) when fission occurs. In a fused state, mitochondria are elongated and share a membrane, and as a result have a larger diameter. A larger size translates to less densely packed mitochondria, producing the lower index of refraction observed in fused mitochondria relative to isolated mitochondria[29,44,45]. Various authors report slightly different diameters for mitochondria that are fused, but all fall around a 0.75 μm figure. The shrinking of the mitochondria in response to fission processes results in a new average diameter of approximately 0.4 μm[22,29,46,47]. Simultaneously, the IOR of a mitochondrion changes from approximately 1.37 to 1.41 as fission occurs and organelles becomes isolated[29,44,45]. The average distance between mitochondria that have undergone fission was estimated to be approximately 3 μm via inspection of images produced in various studies, like those conducted by Zhang et al shown in Figure 2[29,42].

Utilizing the aforementioned data in MATLAB, I randomly generate a specified number of mitochondrial chains (a user input) containing a variable number of mitochondria (uniform

distribution about a mean of 6 mitochondria per chain[29,42]) in a 50x50x50 volume, representing a potential sample of imaged retinal tissue. The chains are built parallel to one another but distributed within the "tissue," modeling the average observed orientation of mitochondrial chains in retinal cells, where the chains run along the same axis as the length of the cell body[48]. Each individual mitochondrion is assigned a diameter that is normally distributed about the average diameter observed in fused states of 0.75 μm ($\sigma = 0.05$ μm). Additionally, each mitochondrion is randomly assigned an index of refraction normally distributed about 1.37 ($\sigma = 0.01$ μm), the average IOR observed in fused mitochondria. The randomly generated 3-dimensional coordinates for each mitochondrion are stored. There is a minimum distance between mitochondrial chains imposed that constrains the number of chains that can be "built" in the given volume. This distance was roughly assigned and is related to the diameter of the largest mitochondrion.

The user then inputs a desired number of "frames" that will dictate the number of steps that are taken towards a state of complete fission. For instance, if the user inputs a value of 100 for "frames" there will be 100 images generated, where each subsequent image represents an additional 1% movement towards fission. Using vector calculations, the model estimates the "shape" or "linearity" of each mitochondrial chain. Adding some variability to this shape with each step, but maintaining an overall linear directionality, new coordinates are calculated for each mitochondrion in each frame. Along with a physical movement within the model volume comes a change in the diameter and IOR for each mitochondrion, depending upon the diameter and IOR of the previous frame, and trending towards the values of diameter and IOR noted in fully isolated mitochondria. This is how "memory" is incorporated in the model.

The mitochondria are modeled as spheres. The color of each sphere, or mitochondrion, is

mapped to its respective index of refraction. Lower and higher indices of refraction correspond to blue and green, respectively. So, the lower the IOR the bluer the sphere appears, or the higher the IOR the greener the sphere appears. The relative diameters can also be observed in each frame.

See Appendix A for the relevant code.

4.1.2 Light Scattering Profile Generator

At this point, the second component of my research became relevant. Prior to building the Monte Carlo model, I built a MATLAB program that could output light scattering profiles when passed specific parameters regarding a spherical scatterer and the medium through which the light travels. As mentioned previously, Mie Theory describes and defines the way that spheres scatter light in a medium. Because the mitochondria may be in a fusion state, simulating light scattering by a single sphere is an approximation and does not account for interactions between neighboring mitochondria. Parameters affecting light scattering profiles when light interacts with dispersed spherical scatterers are: wavelength of incident light, diameter of scatterer, IOR of the medium, IOR of the scatterer, concentration of the scatterers within the medium and the number of angles[49]. These parameters were made inputs to my program.

Consider a point light source, a spherical scattering particle, and an observer whose three positions define a plane called the scattering plane. Incident and scattered light can be reduced to their components that are parallel and perpendicular to the defined scattering plane. If you average these two components for scattered light, you produce natural values that correspond to the relative intensity of scattered light at each angle[49]. These natural values can be mapped on a polar plot to produce a light scattering profile. If you plot the radial distance values corresponding to relative intensity on a log scale you can generate a slightly different polar plot

that allows for a better visualization of side lobes in the scattering profile.

The Oregon Medical Laser Center previously created a Mie Scattering Calculator that allows you to input the mentioned parameters[50]. The limitation of this online calculator is that you have to change parameters and generate data/scattering profiles one by one. In order to solve this problem, I utilized the code they provided on their website for the calculator and optimized it to function as a program in MATLAB that receives the parameters in sets. The code I optimized and created calculates the natural values and maps the corresponding light scattering profiles on a log scale. See Appendix A for the relevant code.

4.1.2 Intersection of Monte Carlo Model and Scattering Profile Generator

After completing both sets of code, I wanted to combine the two. My final model generates two separate plots and shows them in the same figure. The first plot is a specific frame of the Monte Carlo model, showing the overall morphology of the independent mitochondrial chains. The second plot is a scattering profile. The scattering profile generated is related to each frame of the Monte Carlo model. I randomly select one mitochondrion from the set of mitochondria in the model and track that specific mitochondrion's changes in IOR and diameter over time. I pass that data to the scattering profile generator in each frame and subsequently create a scattering profile. Note that the modeled light is incident from the left.

This combination is useful because it allows us to view and record the simulated changes in overall mitochondrial structure during the progression of Alzheimer's disease. At the same time, we can see how light would scatter upon interaction with a specific mitochondrion, relating changes in light scattering with changes in mitochondrial structure due to the disease.

4.2 Results

The final product of my model is a movie that simulates the progression of the disease. The

user inputs the number of frames desired, as well as a value for frames per second that determines the length of the film.

Below are screenshots of a film showing 50 mitochondrial chains undergoing the fission processes associated with Alzheimer's. Parameters passed to the scattering profile generator to produce the right side of each figure were: the randomly selected mitochondrion's diameter, incident light wavelength of 1050 nm (an OCT relevant wavelength), IOR of medium equal to 1, IOR of randomly selected sphere, angles value of 360 and a concentration of 0.1.

Figure 4 represents steady state, or fusion in the tissue. This would resemble a mitochondrial structure and scattering in a healthy individual. 25%, 50%, 75% and 100% progression towards fission are depicted by figures 5, 6, 7 and 8, respectively.

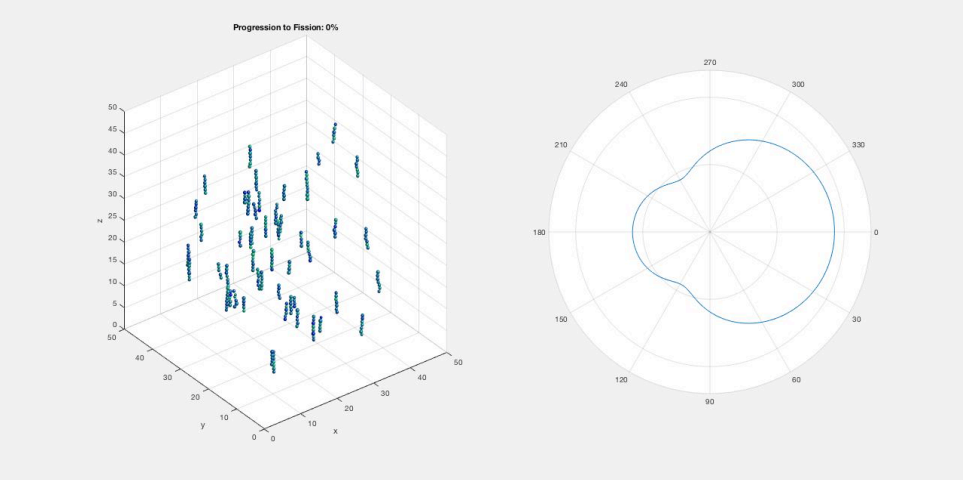

Figure 4: Screenshot from Output of Monte Carlo Model at Steady-State (Progression to Fission = 0%)

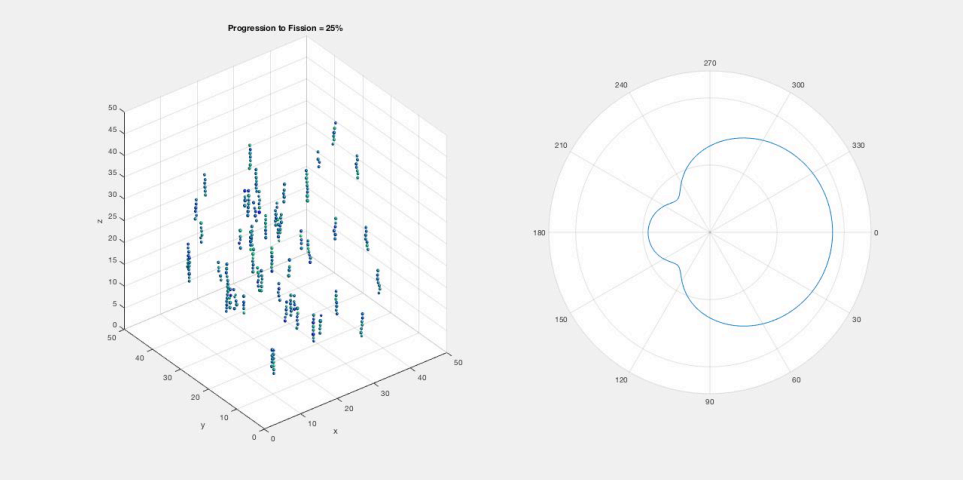

Figure 5: Screenshot from Output of Monte Carlo Model (Progression to Fission = 25%)

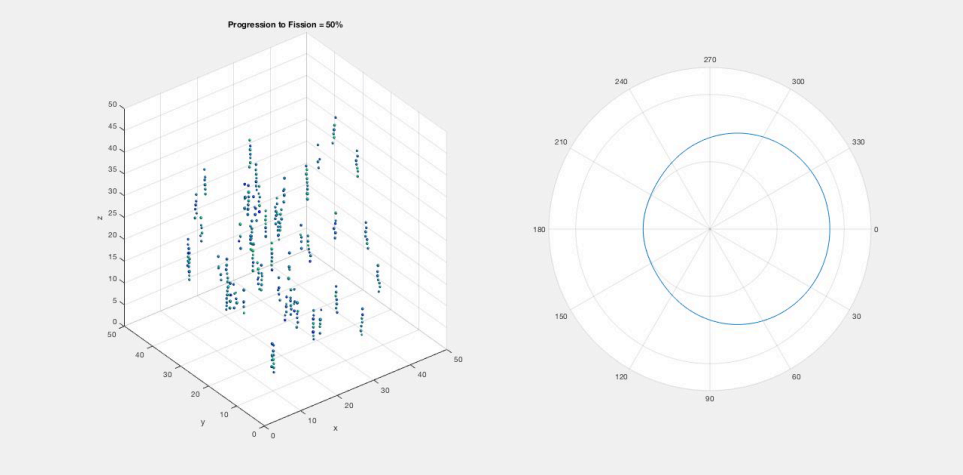

Figure 6: Screenshot from Output of Monte Carlo Model (Progression to Fission = 50%)

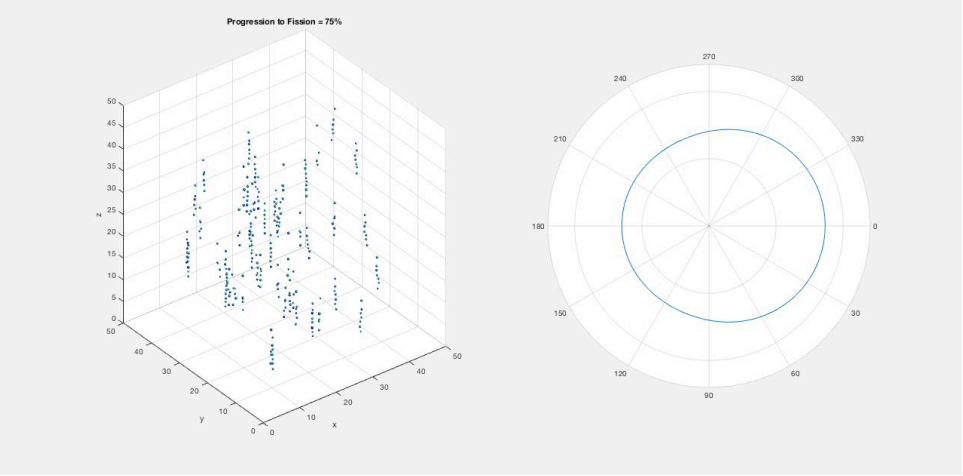

Figure 7: Screenshot from Output of Monte Carlo Model (Progression to Fission = 75%)

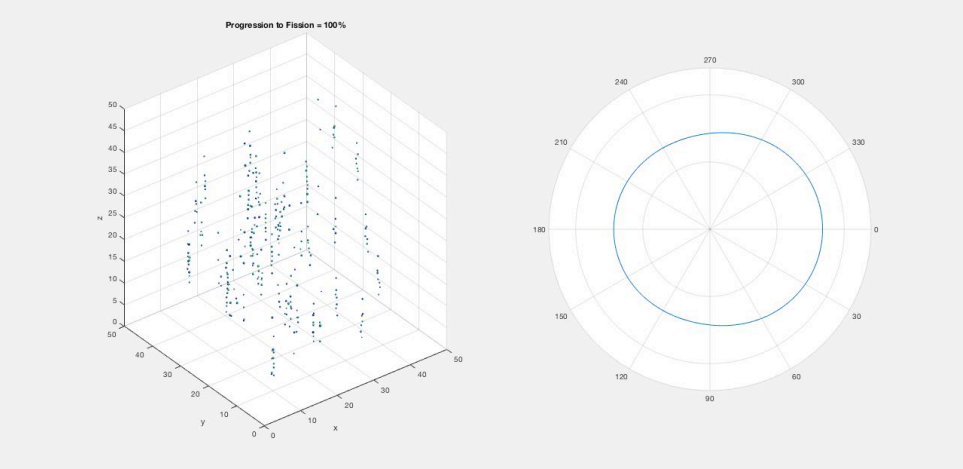

Figure 8: Screenshot from Output of Monte Carlo Model (Progression to Fission = 100%)

I have posted the video corresponding to these screenshots on YouTube. The link is as follows: https://youtu.be/W5CmLAasqqM. The video can also be searched for by typing in the following title: "Modeling Mitochondrial Fission During Alzheimer's Disease."

The left-hand side of each of these figures models closely the structural changes that occur to mitochondria during the fission processes associated with Alzheimer's disease. Simultaneously, the right-hand side shows how the light scattering profiles are affected by these changes. There appears to be a more even distribution of scattering when the scatterer, or mitochondrion, undergoes a decrease in diameter and increase in IOR. This confirms the idea that the backscattered light distribution changes with changes in scatterer properties.

The lab's hypothesis is that mitochondrial fission will result in a relative increase in large angle backscattered light compared to low angle light. The results from this model are consistent and support this hypothesis. However, a limitation of the model is that we are currently only able to predict light scattering from a single mitochondrion and not include effects from interacting units.

4 Conclusion and Future Work

4.1 Concluding Remarks

This model is unique in its ability to predict and simulate physiological changes that are known to occur in the retina during neurodegenerative diseases like Alzheimer's. It is also useful in that it allows us to create a rudimentary prediction of how light would interact with a specific mitochondrion within a sample that is being imaged. Further, the model provides us with a better understanding of what to expect from optical imaging of the retina during a disease like Alzheimer's.

The future development and application of this model has the potential to provide the "controlled, expected results" we might want to compare with those we experimentally acquire in lab, using a murine model. In addition, having a computational model that can predict how the OCT signal would vary with disease state is a more ethical first step than using an animal model to gather the same data.

4.1 Future Work

This model and its applications still stand to be developed further. Namely, we might be able to use it in the future to identify the wavelength-dependence of the scatterers in the model "volume." This would allow us to generate SARi and SARi"" data, which could be used to map trends that would help us identify the relevant sub-resolution light-scattering variations that are occurring during Alzheimer's. For instance, we could potentially create a lookup table where the axes are SARi and SARi''. The intersection of various combinations of SARi and SARi'' could contain information about mitochondrial size/structure. This information about mitochondrial structure could help us identify a relevant disease state. We could also experimentally confirm

this table and this model by building phantoms with a medium in which scatterers are dispersed.

If this does become possible and we ultimately predict light scattering from multiple interacting scatterers as opposed to non-interacting units, we would have a more robust model with many more clinical applications. We could create a similar lookup table that would serve as a heuristic by which an earlier stage diagnosis could be made. This diagnosis would be earlier than current methods allow for because variations in mitochondrial dynamics occur in the earliest stages of the disease (preclinical). Additionally, this technique would be non-invasive and therefore has the potential to become a part of a standard check-up in at risk patient populations.

In order to make the model more robust, further literature review should be conducted as more information regarding the relationship between mitochondrial morphology and Alzheimer's comes to light. This would allow for the integration of more parameters that would make the model more accurate in simulating the changes that occur in vivo. The code I have written can also be improved by adding any additional complexity the next user sees fit.

In all, the future of this "workstream" is bright and is meant to be continued by other investigators.

References

1. Reitz, C. & Mayeux, R. Alzheimer disease: Epidemiology, diagnostic criteria, risk factors and biomarkers. *Biochem. Pharmacol.* **88,** 640–651 (2014).
2. Alzheimer's Association. Latest Alzheimer's Facts and Figures. *Latest Facts & Figures Report | Alzheimer's Association* (2013). Available at: http://www.alz.org/facts/overview.asp. (Accessed: 27th April 2017)
3. Hebert, L. E., Weuve, J., Scherr, P. A. & Evans, D. A. Alzheimer disease in the United States (2010-2050) estimated using the 2010 census. *Neurology* **80,** 1778–1783 (2013).
4. The Baby Boom Cohort in the United States: 2012 to 2060 - p25-1141.pdf.
5. Healthy Brain Initiative: Alzheimer's Disease | Healthy Aging | CDC.
6. Aging, N. I. on. Health care costs for dementia found greater than for any other disease. *National Institute on Aging* (2015). Available at: https://www.nia.nih.gov/newsroom/2015/10/health-care-costs-dementia-found-greater-any-other-disease. (Accessed: 27th April 2017)
7. Alzheimer's Association. Stages of Alzheimer's & Symptoms | Alzheimer's Association. Available at: http://www.alz.org/alzheimers_disease_stages_of_alzheimers.asp. (Accessed: 27th April 2017)
8. National Institute of Health. Alzheimer's Disease Fact Sheet. *National Institute on Aging* (2011). Available at: https://www.nia.nih.gov/alzheimers/publication/alzheimers-disease-fact-sheet. (Accessed: 27th April 2017)
9. Burns, A. & Iliffe, S. Alzheimer's disease. *BMJ* **338,** b158–b158 (2009).
10. Brunnström, H. R. & Englund, E. M. Cause of death in patients with dementia disorders. *Eur. J. Neurol.* **16,** 488–492 (2009).

11. Amyloid Plaques and Neurofibrillary Tangles. *BrightFocus Foundation* (2015). Available at: http://www.brightfocus.org/alzheimers/infographic/amyloid-plaques-and-neurofibrillary-tangles. (Accessed: 9th May 2017)
12. Brion, J. P. Neurofibrillary tangles and Alzheimer's disease. *Eur. Neurol.* **40,** 130–140 (1998).
13. Murphy, M. P. & LeVine, H. Alzheimer's Disease and the β-Amyloid Peptide. *J. Alzheimers Dis. JAD* **19,** 311 (2010).
14. Rabinovici, G. D. *et al.* Increased metabolic vulnerability in early-onset Alzheimer's disease is not related to amyloid burden. *Brain* **133,** 512–528 (2010).
15. Mitochondrial Fission, Fusion, and Stress | Science. Available at: http://science.sciencemag.org/content/337/6098/1062. (Accessed: 9th May 2017)
16. Chan, D. C. Fusion and Fission: Interlinked Processes Critical for Mitochondrial Health. *http://dx.doi.org/10.1146/annurev-genet-110410-132529* (2012). Available at: http://www.annualreviews.org/doi/10.1146/annurev-genet-110410-132529. (Accessed: 9th May 2017)
17. Chen, H., McCaffery, J. M. & Chan, D. C. Mitochondrial Fusion Protects against Neurodegeneration in the Cerebellum. *Cell* **130,** 548–562 (2007).
18. Okamoto, K. & Shaw, J. M. Mitochondrial Morphology and Dynamics in Yeast and Multicellular Eukaryotes. *http://dx.doi.org/10.1146/annurev.genet.38.072902.093019* (2005). Available at: http://www.annualreviews.org/doi/10.1146/annurev.genet.38.072902.093019. (Accessed: 9th May 2017)

19. Hoppins, S. & Nunnari, J. The molecular mechanism of mitochondrial fusion. *Biochim. Biophys. Acta* **1793,** 20–26 (2009).

20. Chang, C.-R. & Blackstone, C. Dynamic regulation of mitochondrial fission through modification of the dynamin-related protein Drp1. *Ann. N. Y. Acad. Sci.* **1201,** 34–39 (2010).

21. Zhao, J., Lendahl, U. & Nistér, M. Regulation of mitochondrial dynamics: convergences and divergences between yeast and vertebrates. *Cell. Mol. Life Sci.* **70,** 951–976 (2013).

22. Kageyama, Y., Zhang, Z. & Sesaki, H. Mitochondrial division: molecular machinery and physiological functions. *Curr. Opin. Cell Biol.* **23,** 427–434 (2011).

23. Manczak, M., Calkins, M. J. & Reddy, P. H. Impaired mitochondrial dynamics and abnormal interaction of amyloid beta with mitochondrial protein Drp1 in neurons from patients with Alzheimer's disease: implications for neuronal damage. *Hum. Mol. Genet.* **20,** 2495–2509 (2011).

24. Mitophagy: mechanisms, pathophysiological roles, and analysis. Available at: https://www.ncbi.nlm.nih.gov/pmc/articles/PMC3630798/. (Accessed: 9th May 2017)

25. Toyama, E. Q. *et al.* AMP-activated protein kinase mediates mitochondrial fission in response to energy stress. *Science* **351,** 275–281 (2016).

26. Westermann, B. Bioenergetic role of mitochondrial fusion and fission. *Biochim. Biophys. Acta BBA - Bioenerg.* **1817,** 1833–1838 (2012).

27. Rambold, A. S., Kostelecky, B., Elia, N. & Lippincott-Schwartz, J. Tubular network formation protects mitochondria from autophagosomal degradation during nutrient starvation. *Proc. Natl. Acad. Sci.* **108,** 10190–10195 (2011).

28. Gomes, L. C., Benedetto, G. D. & Scorrano, L. During autophagy mitochondria elongate, are spared from degradation and sustain cell viability. *Nat. Cell Biol.* **13,** 589–598 (2011).

29. Zhang, L. *et al.* Altered brain energetics induces mitochondrial fission arrest in Alzheimer's Disease. *Sci. Rep.* **6,** 18725 (2016).

30. Association Between Midlife Vascular Risk Factors and Estimated Brain Amyloid Deposition. *PubMed Journals* Available at: https://ncbi.nlm.nih.gov/labs/articles/28399252/. (Accessed: 12th May 2017)

31. Alzheimer's Association. Alzheimer's & Dementia Testing Advances | Research Center. *Alzheimer's Association* Available at: http://www.alz.org/research/science/earlier_alzheimers_diagnosis.asp. (Accessed: 9th May 2017)

32. Early Diagnosis: The Value of Knowing - 2013_Value_of_Knowing_-_PUBLIC_HEALTH1.pdf.

33. Fujimoto, J. G., Pitris, C., Boppart, S. A. & Brezinski, M. E. Optical Coherence Tomography: An Emerging Technology for Biomedical Imaging and Optical Biopsy. *Neoplasia N. Y. N* **2,** 9–25 (2000).

34. - Optician. Available at: https://www.opticianonline.net/cet-archive/153. (Accessed: 12th May 2017)

35. Haseda, K. *et al.* Significant correlation between refractive index and activity of mitochondria: single mitochondrion study. *Biomed. Opt. Express* **6,** 859–869 (2015).

36. London, A., Benhar, I. & Schwartz, M. The retina as a window to the brain-from eye research to CNS disorders. *Nat. Rev. Neurol.* **9,** 44–53 (2013).

37. Maresca, A., la Morgia, C., Caporali, L., Valentino, M. L. & Carelli, V. The optic nerve: a 'mito-window' on mitochondrial neurodegeneration. *Mol. Cell. Neurosci.* **55,** 62–76 (2013).

38. Archibald, N. K., Clarke, M. P., Mosimann, U. P. & Burn, D. J. The retina in Parkinson's disease. *Brain* **132,** 1128–1145 (2009).

39. Guo, L., Duggan, J. & Cordeiro, M. F. Alzheimer's disease and retinal neurodegeneration. *Curr. Alzheimer Res.* **7,** 3–14 (2010).

40. Petzold, A. *et al.* Optical coherence tomography in multiple sclerosis: a systematic review and meta-analysis. *Lancet Neurol.* **9,** 921–932 (2010).

41. Wang, B. *et al.* Path-length-multiplexed scattering-angle-diverse optical coherence tomography for retinal imaging. *Opt. Lett.* **38,** 4374–4377 (2013).

42. Cagalinec, M. *et al.* Principles of the mitochondrial fusion and fission cycle in neurons. *J Cell Sci* **126,** 2187–2197 (2013).

43. Wang, X. *et al.* Impaired Balance of Mitochondrial Fission and Fusion in Alzheimer's Disease. *J. Neurosci.* **29,** 9090–9103 (2009).

44. Haseda, K. *et al.* Significant correlation between refractive index and activity of mitochondria: single mitochondrion study. *Biomed. Opt. Express* **6,** 859–869 (2015).

45. Drezek, R., Dunn, A. & Richards-Kortum, R. Light scattering from cells: finite-difference time-domain simulations and goniometric measurements. *Appl. Opt.* **38,** 3651–3661 (1999).

46. Cataldo, A. M. *et al.* Abnormalities in mitochondrial structure in cells from patients with bipolar disorder. *Am. J. Pathol.* **177,** 575–585 (2010).

47. Campello, S. & Scorrano, L. Mitochondrial shape changes: orchestrating cell pathophysiology. *EMBO Rep.* **11,** 678–684 (2010).

48. Kolb, H. in *Webvision: The Organization of the Retina and Visual System* (eds. Kolb, H., Fernandez, E. & Nelson, R.) (University of Utah Health Sciences Center, 1995).

49. Bohren, C. & Huffman, D. *Absorption and Scattering of Light by Small Particles*. (John Wiley & Sons, 1983).
50. Mie Scattering Calculator. Available at: http://omlc.org/calc/mie_calc.html. (Accessed: 10th May 2017)

Appendix A: MATLAB code

1) chain_maker_final.m

The main code that calls the other necessary functions

```
%% clear/initialize workspace
clc;
clear all;

chainnum = 50;
lowerbnd = 5;                   %variables to be passed to centerpoints.m

                    %parameters passed to scattering profile generator
lambda = 1050;      %wavelength of incident light (OCT relevant); units=nm
nmed = 1;           %IOR of medium
angles = 360;
conc = .1;          %scatterer concentration

%% we first need to decide how many mitochondria are within each chain
%  and determine the average chain length


for i=1:chainnum
    avg_num = normrnd(6,1); %avg number of mito in chain is ~6
                            % see bioenergetics paper
    mito_num = round(avg_num);  %needs to be discrete
    chain_nums(i,1) = mito_num;
end


% create data for individual mitochondria
% each row corresponds in this matrix is a single chain's mito's
for j=1:length(chain_nums)
for i=1:chain_nums(j,1)
    mito_diams(j,i) = normrnd(.75,.05);     %diameters for each mito w/in
chains
    mito_ior(j,i) = normrnd(1.37,.01);        %index of refraction for each
mito w/in chains
                                            %high end of overall cell..
                                            %approaches 1.41 when isolated
end
end

maxd = max(max(mito_diams));
maxl = max(sum(mito_diams'));
%% variability in the z direction (state=0)
%  will depend on the imported centerpoints from centerpoints code

centers = centerpoints(chainnum, lowerbnd, maxd, maxl);
bottom = centers(:,3) - lowerbnd;
z(:,1) = bottom + 1/2*mito_diams(:,1);      %find the z of centerpoint for
1st mito
for i=2:max(chain_nums)
    z(:,i) = z(:,i-1) + 1/2*mito_diams(:,i-1) + 1/2*mito_diams(:,i); %create
```

```
next z
end
diam_zeros = find(mito_diams==0);
for i=1:length(diam_zeros)
    element = diam_zeros(i);
    z([element]) = 0;
end

%% variability in the x direction
x(:,1) = centers(:,1);
for i=2:max(chain_nums)
    x(:,i) = normrnd(x(:,i-1),1/250*x(:,1));
end
for i=1:length(diam_zeros)
    element = diam_zeros(i);
    x([element]) = 0;
end

%% variability in the y direction
y(:,1) = centers(:,2);
for i=2:max(chain_nums)
    y(:,i) = normrnd(y(:,i-1),1/250*y(:,1));
end
for i=1:length(diam_zeros)
    element = diam_zeros(i);
    y([element]) = 0;
end
%% fission processes INPUTS!!
maxf = 3;     %max fission distance (um) for disjointed mitos
frames = 40;
t = .1;


%% individual mitochondria data pull
test_mito=zeros(frames+1,2);
test_mito(1,1)=mito_diams(1,1);
test_mito(1,2)=mito_ior(1,1);

%% plot specific spheres for t=0
[a,b,c] = sphere;
subplot(1,2,1);
for i=1:size(x,1)
for j=1:size(x,2)
    if x(i,j)~=0&&y(i,j)~=0&&z(i,j)~=0
        xx = a/2*mito_diams(i,j)+x(i,j); %scaled/translated x
        yy = b/2*mito_diams(i,j)+y(i,j); %scaled/translated y
        zz = c/2*mito_diams(i,j)+z(i,j); %scaled/translated z
        col = ones(size(zz))*(mito_ior(i,j)/1.42);
        surf(xx,yy,zz,col,'edgecolor','none');
        hold on
    end
end
end


grid on;
xlabel('x');
```

```
ylabel('y');
zlabel('z');
title('Progression to Fission: 0%');
view(3);
colormap winter
camlight
axis([0 50 0 50 0 50])
subplot(1,2,2);

% User Inputs to Mie Theory
natural = mie_scatter(test_mito(1,1), lambda, nmed, test_mito(1,2), angles,
conc);

nat = natural(2,:);
lognat = log(nat);
polarplot(-(lognat+10))
rlim([0 12]);
ax = gca;
d = ax.ThetaDir
ax.ThetaDir = 'clockwise';
ax.RTick = [0 5 10];
ax.RTickLabel = {' ',' ',' '};


set(gcf, 'Units','pixels','Position',[0 0 1280 640])

F(1) = getframe(gcf);
close all;

%% plot specific spheres during f
close all;

%% plot specific spheres during fission
[a,b,c] = sphere;
t_frame = 1/(frames);
for k=1:frames
ission
[a,b,c] = sphere;
t_frame = 1/(frames);
for k=1:frames
[x,y,z,mito_ior,mito_diams] =
fission(x,y,z,maxf,frames,mito_ior,mito_diams,chain_nums,t);
t_frame_k(k) = t_frame*k*100;
figure;
subplot(1,2,1);
for i=1:size(x,1)
for j=1:size(x,2)
    if x(i,j)~=0&&y(i,j)~=0&&z(i,j)~=0
        xx = a/2*mito_diams(i,j)+x(i,j); %scaled/translated x
        yy = b/2*mito_diams(i,j)+y(i,j); %scaled/translated y
        zz = c/2*mito_diams(i,j)+z(i,j); %scaled/translated z
        col = ones(size(zz))*(mito_ior(i,j)/1.42);
        surf(xx,yy,zz,col,'edgecolor','none');
        hold on
    end
end
end
```

```
grid on;
xlabel('x');
ylabel('y');
zlabel('z');
view(3);
str = sprintf('Progression to Fission = %1.0f%%',t_frame_k(k));
title(str);
colormap winter
camlight
axis([0 50 0 50 0 50])
test_mito(k+1,1)=mito_diams(1,1);
test_mito(k+1,2)=mito_ior(1,1);

subplot(1,2,2);

% User Inputs to Mie Theory
natural = mie_scatter(test_mito(k+1,1), lambda, nmed, test_mito(k+1,2),
angles, conc);
nat = natural(2,:);
lognat = log(nat);
polarplot(-(lognat+10))
rlim([0 12]); %keeps scale of the polar plot consistent
ax = gca;
d = ax.ThetaDir
ax.ThetaDir = 'clockwise';
ax.RTick = [0 5 10];
ax.RTickLabel = {' ',' ',' '};


set(gcf, 'Units','pixels','Position',[0 0 1280 640])
F(k+1) = getframe(gcf);
close all;
end


%% make movie

myVideo = VideoWriter('100mito40frames4fps.avi');
myVideo.FrameRate = 4;
open(myVideo);
writeVideo(myVideo, F);
close(myVideo);
```

2) fission.m

Called during chain_maker_final.m

```
function [x,y,z,mito_ior,mito_diams] =
fission(x,y,z,maxf,frames,mito_ior,mito_diams,chain_nums,varargin)
%% vector calculation component
for i=1:size(x,2)-1
xii = x(:,i+1);
xio = find(xii==0);     %find when an element is 0, bc no vector needed
vx(:,i) = x(:,i+1) - x(:,i);
vx(xio,i) = 0;          %replace incorrect vectors with 0
vy(:,i) = y(:,i+1) - y(:,i);
vy(xio,i) = 0;
vz(:,i) = z(:,i+1) - z(:,i);
vz(xio,i) = 0;
end

%% fission distance a function of t/number of frames
inc_f = maxf/frames;        %incremental distance depending on frames

f_scal = zeros(length(chain_nums),max(chain_nums));
for i=1:size(f_scal,2)
    f_scal(:,i) = i;
end
f_scal = f_scal./chain_nums;

% t=varargin{1};
% poi = t*maxf*frames;              %point of interest, if desired

%% add variability
var_f = inc_f*normrnd(1,maxf/20);   %add variability to incremental f
var_vx = vx*normrnd(1,max(max(abs(vx)))/20);
var_vy = vy*normrnd(1,max(max(abs(vy)))/20);
var_vz = vz*normrnd(1,max(max(abs(vz)))/20);

%% movement
opt = randi(2,1);
if opt == 1                 %leave bottom mito fixed
    var_ff = var_f*f_scal;
    var_ff = var_ff(:,2:size(x,2));
    %x
    xk = x(:,1);
    xx = x(:, 2:size(x,2));
    xx = var_vx.*var_ff/5+xx;
    x = [xk,xx];
    %y
    yk = y(:,1);
    yy = y(:, 2:size(y,2));
    yy = var_vy.*var_ff/5+yy;
    y = [yk,yy];
    %z
    zk = z(:,1);
    zz = z(:, 2:size(z,2));
    zz = var_vz.*var_ff+zz;
    z = [zk,zz];
end
```

```
if opt == 2                %leave top mito fixed
    f_scal = flip(f_scal,2);
    var_ff = var_f*f_scal;
    var_ff = var_ff(:,1:size(x,2)-1);
    %x
    xk = x(:,size(x,2));
    xx = x(:, 1:size(x,2)-1);
    var_vx = var_vx*-1;
    xx = var_vx.*var_ff/5+xx;
    x = [xx,xk];
    %y
    yk = y(:,size(y,2));
    yy = y(:, 1:size(y,2)-1);
    var_vy = var_vy*-1;
    yy = var_vy.*var_ff/5+yy;
    y = [yy,yk];
    %z
    zk = z(:,size(z,2));
    zz = z(:, 1:size(z,2)-1);
    var_vz = var_vz*-1;
    zz = var_vz.*var_ff+zz;
    z = [zz,zk];
end

%% mitochondrial changes
mito_mask = mito_ior;
mito_mask(mito_mask>0) = 1;
%Index of Refraction changes to become higher when isolated
IR_column = 1.37;
IR_isolated = 1.41;
deltaIR = IR_isolated-IR_column; %columnar IOR is lower than isolated
mitochondria
deltaIR = deltaIR/frames; %stepwise change in IR
mito_ior = mito_ior+deltaIR*normrnd(1,.01);
mito_ior = mito_ior.*mito_mask;

%diameters become smaller (from .75 to ~.4)
diam_column = .75;
diam_isolated = .4;
delta_diam = diam_isolated-diam_column;
delta_diam = delta_diam/frames;
mito_diams = mito_diams+delta_diam*normrnd(1,.075);
mito_diams = mito_diams.*mito_mask;

end
```

3) mie_scatter.m

Called by chain_maker_final.m

```
function natural = mie_scatter(dia, lambda, nmed, nsph, angles, conc)
%dia = [um]; lambda = [nm]

    angles=angles;                          %SARis
    nmed = nmed     ;                       % medium refractive index (water)
    npar_real = real(nsph) ;                % particle refractive index
(polystyrene)
    npar_imag = imag(nsph)   ;              % imaginary component of npar
    vf    = 0.05     ;                      % volume fraction of spheres in
medium (analogous to concentration)
                                            %%%%% volume of sphere = (4/3)*pi^3

    m1 = npar_real + npar_imag  ;           % (complex) refractive index of the
spheres
    m = m1/nmed                 ;           % m - relative (to the medium)
complex refractive index
    sa = linspace(-179,180,angles)          ;       % scattering angle range -
- add linspace

    lambda_nm = [lambda]             ;     % [nm] wavelength of incident beam,
we can also set this as a range
    lambdalambda = lambda_nm/1000  ;        % [um] wavelength of incident beam
    diadia = [dia]                 ;        % [um] sphere diameter, we can also
set this as a range
    % Calculates: Size parameter and Scattering Efficiency
    k = (2*pi)/lambdalambda ;           %calculate wave number
    sphr_rad = diadia/2     ;           %calculate sphere radius [um]
    sp = k*sphr_rad         ;           %calculate sp
    sp_nmed = sp*nmed       ;           %the site has this equation for the sp,
so we will us it as well
    x = sp_nmed             ;           %also denote "x" as size parameter
    result_1 = Mie(m,x) ;
    qsca=result_1(5);

%%
% This [for loop] is really only applicable (???) when running through a
range of
% diameters and wavelengths

musgp = zeros(length(lambdalambda),length(diadia),3);

for j=1:length(diadia)
    dia = diadia(j);

    for i=1:length(lambdalambda)
        lambda = lambdalambda(i);

        for k = 1:length(lambdalambda)
            x(k) = (2*pi)/lambda ;
        end

        musgp(i,j,:) = getMieScatter(lambda, dia, vf, m,nmed);
```

```
    end % i

end % j
 x = sp_nmed             ;       %also denote "x" as size parameter

 %% Calculate S1, S2 and Natural

for i = 1:length(sa) ;

    u(i) =   cosd(sa(i))     ;

    S1S2 = Mie_S12(m,x,u(i)) ;
    S1(i)=S1S2(1);
    S2(i)=S1S2(2);

    natural(i) = (abs(S1(i)^2)+abs(S2(i)^2))/(pi*((sp_nmed)*(sp_nmed))*qsca)
;
    NATURAL(i) = [natural(i)] / 2   ;

end


%set up correspondance matrix
    Matrix_saNatural = zeros(2,angles)    ;
    Matrix_saNatural(1,:) = sa          ;
    Matrix_saNatural(2,:) = NATURAL     ;

    natural = Matrix_saNatural;

function result = Mie(m, x)
%The following text lists the Program to compute the Mie Efficiencies:

% Computation of Mie Efficiencies for given
% complex refractive-index ratio m=m'+im"
% and size parameter x=k0*a, where k0= wave number in ambient
% medium, a=sphere radius, using complex Mie Coefficients
% an and bn for n=1 to nmax,
% s. Bohren and Huffman (1983) BEWI:TDD122, p. 103,119-122,477.
% Result: m', m", x, efficiencies for extinction (qext),
% scattering (qsca), absorption (qabs), backscattering (qb),
% asymmetry parameter (asy=<costeta>) and (qratio=qb/qsca).
% Uses the function "Mie_abcd" for an and bn, for n=1 to nmax.
% C. M‰tzler, May 2002.
if x==0 % To avoid a singularity at x=0
result=[real(m) imag(m) 0 0 0 0 0 0 1.5];
elseif x>0 % This is the normal situation
nmax=round(2+x+4*x^(1/3));
n1=nmax-1;
n=(1:nmax);cn=2*n+1; c1n=n.*(n+2)./(n+1); c2n=cn./n./(n+1);
x2=x*x;
f=Mie_abcd(m,x);
anp=(real(f(1,:))); anpp=(imag(f(1,:)));
bnp=(real(f(2,:))); bnpp=(imag(f(2,:)));
g1(1:4,nmax)=[0; 0; 0; 0]; % displaced numbers used for
g1(1,1:n1)=anp(2:nmax); % asymmetry parameter, p. 120
```

```
g1(2,1:n1)=anpp(2:nmax);
g1(3,1:n1)=bnp(2:nmax);
g1(4,1:n1)=bnpp(2:nmax);
dn=cn.*(anp+bnp);
q=sum(dn);
qext=2*q/x2;
en=cn.*(anp.*anp+anpp.*anpp+bnp.*bnp+bnpp.*bnpp);
q=sum(en);
qsca=2*q/x2;
qabs=qext-qsca;
fn=(f(1,:)-f(2,:)).*cn;
gn=(-1).^n;
f(3,:)=fn.*gn;
q=sum(f(3,:));
qb=q*q'/x2;
asy1=c1n.*(anp.*g1(1,:)+anpp.*g1(2,:)+bnp.*g1(3,:)+bnpp.*g1(4,:));
asy2=c2n.*(anp.*bnp+anpp.*bnpp);
asy=4/x2*sum(asy1+asy2)/qsca;
qratio=qb/qsca;
result=[real(m) imag(m) x qext qsca qabs qb asy qratio];
end;
function S1S2 = Mie_S12(m,x,u)
% Computation of Mie Scattering functions S1 and S2
% for complex refractive index m=m'+im",
% size parameter x=k0*a, and u=cos(scattering angle),
% where k0=vacuum wave number, a=sphere radius;
% s. p. 111-114, Bohren and Huffman (1983) BEWI:TDD122
% C. M%tzler, May 2002

nmax=round(2+x+4*x^(1/3));
abcd=Mie_abcd(m,x);             %compute the bessel coefficients
an=abcd(1,:);
bn=abcd(2,:);
pt=Mie_pt(u,nmax);
pin =pt(1,:);
tin=pt(2,:);
n=(1:nmax);
n2=(2*n+1)./(n.*(n+1));
pin=n2.*pin;
tin=n2.*tin;
S1=(an*pin'+bn*tin');
S2=(an*tin'+bn*pin');


S1S2=[S1;S2];
function result = Mie_abcd(m, x)
%The following text lists the basic program to compute the Mie Coefficients
an, bn,
%cn, dn and to produce a matrix of nmax column vectors [an; bn; cn; dn]:

% Computes a matrix of Mie coefficients, a_n, b_n, c_n, d_n,
% of orders n=1 to nmax, complex refractive index m=m'+im",
% and size parameter x=k0*a, where k0= wave number
% in the ambient medium, a=sphere radius;
% p. 100, 477 in Bohren and Huffman (1983) BEWI:TDD122
% C. M%tzler, June 2002
nmax=round(2+x+4*x^(1/3));
```

```
n=(1:nmax); nu = (n+0.5); z=m.*x; m2=m.*m;
sqx= sqrt(0.5*pi./x); sqz= sqrt(0.5*pi./z);
bx = besselj(nu, x).*sqx;
bz = besselj(nu, z).*sqz;
yx = bessely(nu, x).*sqx;
hx = bx+i*yx;
b1x=[sin(x)/x, bx(1:nmax-1)];
b1z=[sin(z)/z, bz(1:nmax-1)];
y1x=[-cos(x)/x, yx(1:nmax-1)];
h1x= b1x+i*y1x;
ax = x.*b1x-n.*bx;
az = z.*b1z-n.*bz;
ahx= x.*h1x-n.*hx;
an = (m2.*bz.*ax-bx.*az)./(m2.*bz.*ahx-hx.*az);
bn = (bz.*ax-bx.*az)./(bz.*ahx-hx.*az);
cn = (bx.*ahx-hx.*ax)./(bz.*ahx-hx.*az);
dn = m.*(bx.*ahx-hx.*ax)./(m2.*bz.*ahx-hx.*az);
result=[an; bn; cn; dn];
function musgp = getMieScatter(lambda, dia, fv, npar,nmed)
% function musgp = getMieScatter(lambda, dia, fv)
%  fv            = volume fraction of spheres in medium (eg., fv = 0.05)
%  lambda        = wavelength in um (eg., lambda = 0.633)
%  dia           = sphere diameter in um (eg., dia_um = 0.0500)
%  npar          = particle refractive index (eg. polystyrene = 1.57)
%  nmed          = medium refractive index (eg., water = 1.33)
%                  Note: npar and nmed can be imaginary numbers.
%  returns musgp = [mus g musp]
%       mus      = scattering coefficient [cm^-1]
%       g        = anisotropy of scattering [dimensionless]
%       musp     = reduced scattering coefficient [cm^-1]
%  Uses
%       Mie.m, which uses mie_abcd.m, from Maetzler 2002
%
% - Steven Jacques, 2009

Vsphere = 4/3*pi*(dia/2)^3;     % volume of sphere
rho     = fv/Vsphere;           % #/um^3, concentration of spheres

m = npar/nmed;                  % ratio of refractive indices
x = pi*dia/(lambda/nmed);       % ratio circumference/wavelength in medium

u = Mie(m, x)';                 % <----- Matlzer's subroutine
% u = [real(m) imag(m) x qext qsca qabs qb asy qratio];

qsca = u(5);                    % scattering efficiency, Qsca
g    = u(8);                    % anisotropy, g

A       = pi*dia^2/4;           % geometrical cross-sectional area, um^2
sigma_s = qsca*A;               % scattering cross-section, um^2
mus     = sigma_s*rho*1e4;      % scattering coeff. cm^-1
musp    = mus*(1-g);            % reduced scattering coeff. cm^-1

if 1 % 1 = print full report, 0 = disable
    disp('----- choice:')
    disp(sprintf('lambda  \t= %0.3f um', lambda))
    disp(sprintf('dia     \t= %0.3f um', dia))
    disp(sprintf('rho     \t= %0.3f #/um^3', rho))
```

```
    disp(sprintf('npar    \t= %0.3f', npar))
    disp(sprintf('nmed    \t= %0.3f', nmed))
    disp('----- result:')
    disp(sprintf('real(m) \t= %0.3f', u(1)))
    disp(sprintf('imag(m) \t= %0.3e', u(2)))
    disp(sprintf('x       \t= %0.3e', u(3)))
    disp(sprintf('qext    \t= %0.3e', u(4)))
    disp(sprintf('qsca    \t= %0.3e', u(5)))
    disp(sprintf('qabs    \t= %0.3e', u(6)))
    disp(sprintf('qb      \t= %0.3e', u(7)))
    disp(sprintf('asy     \t= %0.4f', u(8)))
    disp(sprintf('qratio  \t= %0.3e', u(9)))
    disp('----- optical properties:')
    disp(sprintf('mus     \t= %0.3f cm^-1', mus))
    disp(sprintf('g       \t= %0.4f', g))
    disp(sprintf('musp    \t= %0.3f cm^-1', musp))
end

musgp= real([mus g musp]);
function result=Mie_pt(u,nmax)
% The following text lists the program to compute a matrix of ?n and ?n
functions for
% n=1 to nmax:
% pi_n and tau_n, -1 <= u= cos? <= 1, n1 integer from 1 to nmax
% angular functions used in Mie Theory
% Bohren and Huffman (1983), p. 94 - 95
p(1)=1;
t(1)=u;
p(2)=3*u;
t(2)=3*cos(2*acos(u));
for n1=3:nmax,
p1=(2*n1-1)./(n1-1).*p(n1-1).*u;
p2=n1./(n1-1).*p(n1-2);
p(n1)=p1-p2;
t1=n1*u.*p(n1);
t2=(n1+1).*p(n1-1);
t(n1)=t1-t2;
end;
result=[p;t];
```

BIOGRAPHY

Stefan Sierra was born in New Orleans, Louisiana on September 15, 1995 but moved to Houston, Texas in August 2005 due to Hurricane Katrina. In August 2012, Stefan enrolled at the University of Texas at Austin where he pursued a dual degree in Biomedical Engineering Honors and Plan II Honors. In the summer between his third and fourth years, Stefan interned in New York City at J.P. Morgan in the Private Bank. In his final summer, Stefan interned at McKinsey and Company, where he will return as a full-time Business Analyst in the fall.